Battery Energy

WILEY

RESEARCH ARTICLE OPEN ACCESS

Real-Time, Interpretable Diagnostics for Solid-State Batteries via Machine Learning on In Situ Impedance Spectra

Zachary Warren[1,2] | Felipe Cuasquer[1,2] | Regina Sanchez[1] | Patricia A. Apellániz[3] | Alejandro Almodóvar[3] | Juan Parras[3] | Nataly Carolina Rosero-Navarro[1]

[1]Instituto de Cerámica y Vidrio – CSIC, Madrid, Spain | [2]Universidad Autónoma de Madrid – Ciudad Universitaria de Cantoblanco, Madrid, Spain | [3]Information Processing and Telecommunications Center, ETSI Telecomunicación, Universidad Politécnica de Madrid, Madrid, Spain

Correspondence: Nataly Carolina Rosero-Navarro (rosero@icv.csic.es)

Received: 5 February 2026 | **Revised:** 13 April 2026 | **Accepted:** 22 April 2026

ABSTRACT

Electrochemical impedance spectroscopy (EIS) is highly sensitive to interfacial processes in solid-state batteries (SSBs) but can be difficult to interpret in real time. Here we pair in situ EIS with machine learning (ML) to create a lightweight, interpretable diagnostic framework. By encoding spectra into feature vectors and training tree-based multi-output regressors, we achieve real-time predictions of state of charge and cycle index with $R^2 > 0.99$. Feature-importance analysis links dominant mid- and low-frequency responses to cathode and anode degradation, respectively. Remarkably, retraining on only five key features maintains sub-percent accuracy, enabling millisecond-scale, impedance-based monitoring suitable for embedded solid-state battery management systems.

1 | Introduction

Electrochemical energy storage is entering an inflection point: electrified transportation, renewables integration, and widespread portable electronics demand batteries that are simultaneously safer, longer-lived, and more energy-dense. Solid-state batteries (SSBs) promise a decisive step forward by replacing flammable liquids with inorganic solid electrolytes and enabling lithium-metal anodes [1–3]. Yet despite impressive progress in materials chemistry and cell engineering, SSBs remain difficult to monitor and control during operation. Interfaces dominate transport and failure [4], mechanical and electrochemical couplings evolve as a function of state of charge (SoC) [5], and the all-solid architecture obscures internal processes. The net result is a device that can look healthy by conventional voltage–current metrics while quietly developing interfacial resistances, voids, or contact loss that precipitate rapid capacity loss or short circuits. What is missing are minimally invasive, information-rich diagnostics that can operate continuously and translate directly into actionable battery management.

Electrochemical impedance spectroscopy (EIS) has long been the most sensitive probe of multi-scale battery physics [5, 6]. By perturbing a cell with a small sinusoid and recording the frequency-dependent response, EIS separates processes by timescale and reveals transport, interfacial charge transfer, and polarization phenomena. In SSBs, where interfaces are the main actors, EIS is uniquely powerful. The challenge is not data generation but interpretation: Nyquist arcs overlap, Bode features shift with cycling, equivalent-circuit selections are subjective, and least-squares fits become fragile when interfacial impedances dominate [6]. These realities have kept EIS largely confined to static characterization and post-mortem analysis rather than real-time control.

Here, we introduce a practical route to real-time, interpretable diagnostics for SSBs by fusing in situ EIS with ML within our proprietary software package, NEVORA (see Disclosure). This framework automatically detects charge and discharge cycles from raw in situ cycle data and transforms each impedance spectrum into a compact, physics-aware feature vector

associated with well-defined states of charge and virtual cycle numbers. Multi-output regression models are then trained to predict SoC and cycle number as a proxy for state of health (SoH), while model interpretation techniques map these predictions back to physically meaningful interfacial and transport processes. Crucially, the approach is designed to be robust against the inherent ambiguity of equivalent-circuit fitting while retaining interpretability—an essential requirement for integration into battery management systems.

1.1 | Experimental Design and Physical Picture

Figure 1 summarizes the operating picture. We study sulfide-based SSBs (Li_6PS_5Cl (LPSC) electrolyte, NMC-111 composite cathode, Li/In anode; Supporting Information: Figure S1a,b) cycled galvanostatically between 2.0 and 4.0 V while acquiring potentiostatic EIS blocks at selected voltages.

In Figure 1, a representative Nyquist spectrum (panel a) reveals multiple depressed semicircles and a low-frequency tail, characteristic of distinct transport and interfacial processes. The corresponding schematic (panel b) and equivalent circuit (panel d) map these features onto bulk, grain-boundary, and interfacial resistances (R_0–R_3). The anode interface (panel c) evolves dynamically with potential, where void formation at low voltages increases R_3. Panel e outlines the in situ protocol used to track spectral and fitted-parameter evolution with state of charge and cycling.

The selected cell configuration (Li_6PS_5Cl electrolyte, NMC-111 composite cathode, and Li/In anode) was chosen as a representative sulfide-based solid-state battery system in which interfacial processes are known to dominate impedance behavior. This architecture provides a well-defined platform for resolving bulk and interfacial contributions, making it particularly suitable for validating impedance-based diagnostic frameworks [7, 8]. Cells were operated under galvanostatic cycling between 2.0 and 4.0 V at current densities of 0.05–0.25 mA. These conditions were selected to balance electrochemical stability with sufficient sensitivity to interfacial evolution, allowing measurable changes in impedance during cycling. The primary objective of this study is not to optimize electrochemical performance, but rather to establish a diagnostic framework under controlled and reproducible conditions where impedance evolution is physically interpretable.

The present study employs a full-cell configuration consisting of a composite NMC cathode and a Li/In alloy anode. The Li/In electrode provides a relatively stable and well-defined electrochemical potential, which simplifies interpretation of impedance features compared to systems with highly dynamic lithium

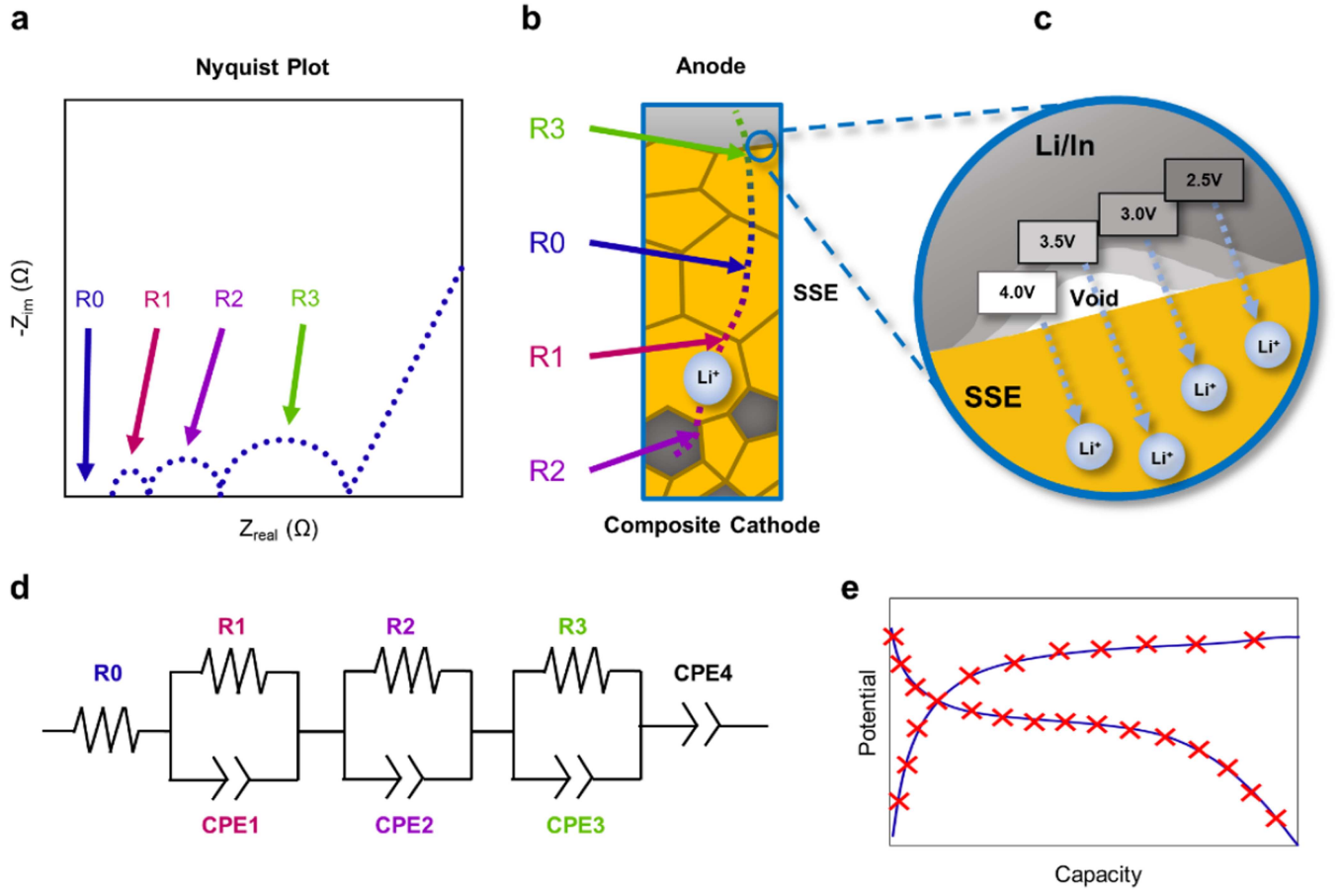

FIGURE 1 | Operating picture and equivalent-circuit framework. (a) Representative Nyquist plot with qualitative assignment of resistive contributions R_0–R_3. (b) Schematic cutaway of the SSB stack, indicating transport pathways and the locations of processes associated with each R term. (c) Illustration of anode-side contact loss and void formation with potential dependency. (d) Equivalent circuit—series R_0 plus three parallel R–CPE elements and a terminal CPE—used for physical interpretation. (e) Experimental schedule: EIS blocks acquired at selected voltages during galvanostatic cycling.

metal interfaces. While this configuration reduces some of the complexity associated with fully symmetric or lithium-metal full cells, the proposed framework is not limited to this specific architecture. In general full-cell configurations, the impedance response reflects coupled contributions from both electrodes, increasing complexity but not precluding application of the method. Because the present approach relies on feature-based representations of the full impedance spectrum rather than explicit separation of individual processes, it can be extended to more complex full-cell systems, where the model learns mappings between spectral features and the global electrochemical state. The framework is inherently adaptable across electrode chemistries and cell architectures via feature adaptation and calibration strategies.

1.2 | From Spectra to Features to State

The feature engineering strategy is guided by the principle of capturing the geometry of the impedance response while maintaining robustness and computational efficiency. Threshold-based features (e.g., counts where |Z| or phase exceed predefined values) provide coarse but highly stable descriptors of spectral shape. Physically, these features approximate the extent of resistive or capacitive dominance across frequency ranges and are particularly sensitive to early-stage interfacial changes. Because they do not rely on peak fitting or precise feature localization, they remain robust under noise and spectral distortion. Extrema, characteristic frequencies, and slopes encode transitions between electrochemical processes and reflect shifts in relaxation times associated with degradation. These features retain direct physical meaning while avoiding assumptions inherent to equivalent-circuit models. Integrated quantities (e.g., areas under Nyquist or Bode curves) act as global descriptors of impedance magnitude and energy dissipation. However, these quantities are often correlated with simpler descriptors such as extrema or low-frequency intercepts and therefore contribute less uniquely to model performance. This hybrid feature design intentionally combines low-cost descriptors, physically interpretable quantities, and global geometric summaries to ensure both robustness and interpretability. In contrast to equivalent-circuit or DRT approaches, which seek to decompose the impedance response into discrete processes, the present feature design treats the spectrum as a continuous geometric object, where physically meaningful descriptors capture its shape, extent, and transitions without requiring unique process separation.

For modeling, NEVORA uses two complementary, off-the-shelf ensemble regressors in a multi-output configuration—Random Forest (RF) and Gradient Boosting (GB)—to predict SoC (%) and cycle number simultaneously from a single feature vector. Tree ensembles are a natural choice: they capture non-linear interactions, handle mixed-scale features without normalization, and provide straightforward feature-importance measures for interpretability [9]. Models are trained on a 70/30 split of vectorized spectra; performance is quantified by R^2 and mean absolute error (MAE). It is important to note that each prediction is performed on a single impedance spectrum corresponding to a specific operating point. Although the data are collected sequentially during cycling, the modeling task is formulated as a pointwise regression problem rather than a temporal sequence prediction. Consequently, models designed for sequential data (e.g., recurrent neural networks such as LSTM or GRU) do not provide a natural advantage in this context. Given the moderate data set size and the structured, tabular nature of the feature vectors, tree-based methods provide a favorable balance between predictive performance, robustness, and interpretability.

1.3 | Performance and Interpretability

Figure 2 summarizes the quantitative performance and physical interpretability of the machine-learning models. Figure 2a–d shows predicted versus experimental values for the held-out test set. Both GB and RF models exhibit near-ideal diagonal correlations for cycle number and state of charge (SoC), with coefficients of determination exceeding 0.99 and mean absolute errors below 1% (Table 1). Deviations remain limited even at low SoC and during early cycling stages, where interfacial evolution is most pronounced.

These metrics indicate a high goodness-of-fit, comparable to the quality criteria typically reported for equivalent-circuit modeling of impedance spectra, confirming that the extracted impedance features reliably capture the electrochemical state of the system.

Figure 2e presents the RF feature importances, highlighting the dominant contribution of cell potential and selected phase-angle components (e.g., Phase_21). This result is physically meaningful: the phase response reflects the balance between resistive and capacitive processes across frequency and is highly sensitive to interfacial phenomena, while the cell potential governs the interfacial state and space-charge configuration [10]. The strong predictive performance therefore arises from physically relevant descriptors rather than purely statistical correlations, which together capture both the thermodynamic state and the evolving interfacial processes within the cell.

1.4 | Linking ML Outputs to Equivalent-Circuit Evolution

While NEVORA does not require circuit fitting, the spectra can nevertheless be fitted to an equivalent circuit model (such as the one illustrated in Figure 1d) to validate underlying physical interpretation. Here, ECM fitting is used strictly as a qualitative interpretive tool rather than a predictive framework, highlighting the distinction between mechanistic interpretation and diagnostic inference. This distinction is critical, as the proposed approach avoids reliance on circuit parameterization for state estimation while still leveraging ECMs to contextualize spectral evolution.

R_2 (cathode–electrolyte interface ~794 Hz) grows with cycling and at high potentials, consistent with capacity fade; R_3 (anode interface) increases sharply at low voltages where voids and contact loss are likely; and R_0 and R_1 (bulk and grain boundary) remain comparatively stable except for occasional artifacts, which become more noticeable at high potentials. These trends are evident in the systematic evolution of the Bode phase spectra (Figure 4) and the corresponding qualitative changes in Nyquist curvature (Figure 3a), indicating progressive modification of interfacial processes during cycling and contributing to the capacity fade observed in Supporting Information: Figure S2a,b. The consistency of these spectral trends across the data set supports

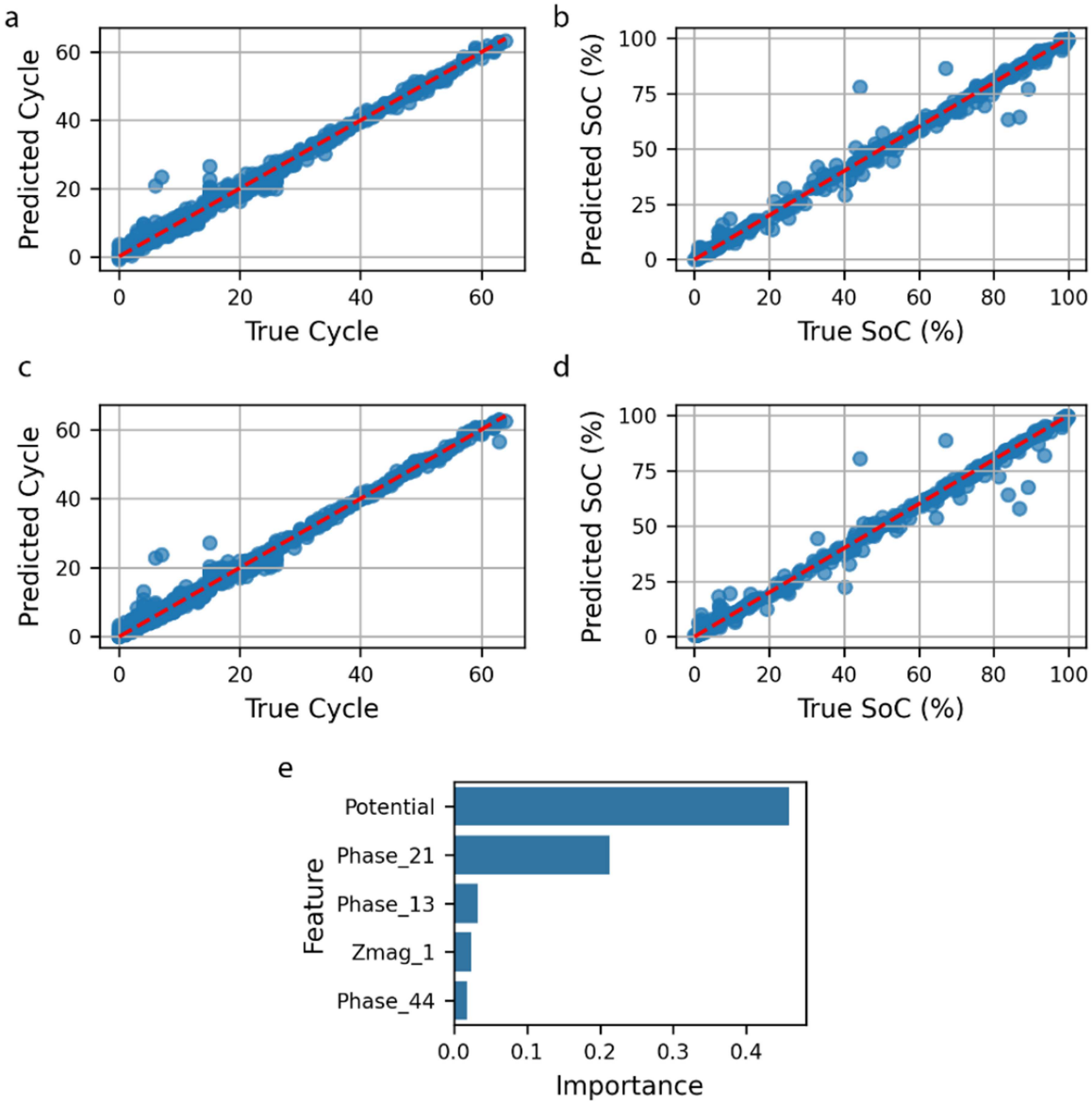

FIGURE 2 | Model performance and interpretability. (a) Predicted versus true cycle number (Gradient Boosting). (b) Predicted versus true state of charge (SoC) (Gradient Boosting). (c) Predicted versus true cycle number (Random Forest). (d) Predicted versus true SoC (Random Forest). (e) Random-Forest feature importances, highlighting dominant roles for potential and selected phase-angle features.

TABLE 1 | Performance metrics of machine-learning models trained on EIS-derived feature vectors for predicting the state of charge (SoC) and cycle number. Both Random Forest and Gradient Boosting regressors exhibit excellent predictive accuracy, with coefficients of determination ($R^2 > 0.99$) and mean absolute errors (MAE) below 1%, confirming the strong correlation between impedance features and solid-state battery state evolution.

Model	Target	R^2	MAE
Random Forest	SoC (%)	0.994	0.915
Random Forest	Cycle	0.991	0.881
Gradient boosting	SoC (%)	0.995	0.949
Gradient boosting	Cycle	0.992	0.919

the ML interpretation, whereby the most informative features are those that track the development of the interfacial arc.

1.5 | A Closer Look at the Spectra

The Bode-phase evolution in Figure 4 encapsulates how impedance carries state information. At fixed potentials (2, 3.1, 4 V) across cycles, the mid-frequency phase peak (794 Hz)—associated with a composite-cathode interfacial process—systematically increases and shifts to lower frequency with aging (up-arrows), while the low-frequency phase decreases (down-arrows), signaling reduced capacitive storage or contact at the anode side and the inverse at the cathode interface. When

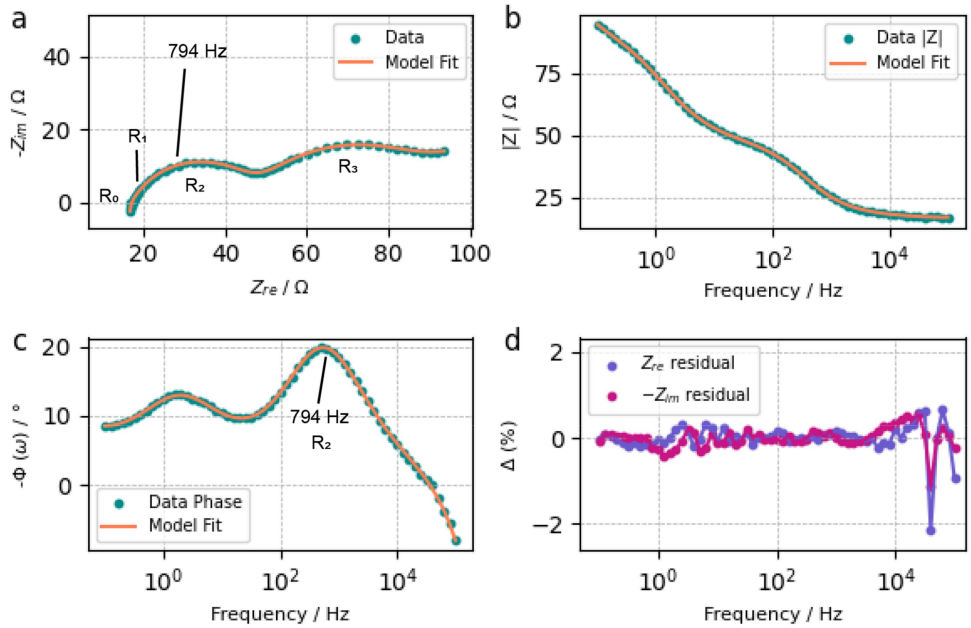

FIGURE 3 | Representative electrochemical impedance spectroscopy (EIS) spectrum and model fit extracted at 3.2 V during the third cycle. (a) Nyquist plot ($-Z_{im}$ vs. Z_{re}) showing experimental data and equivalent-circuit fit, with labeled resistive components R_0–R_3 corresponding to bulk, grain-boundary, and interfacial processes. (b) Bode magnitude plot and (c) Bode phase plot highlighting the main relaxation feature near 794 Hz, attributed to the cathode–electrolyte interface (R_2). (d) Percentage residuals of the real and imaginary components confirm the quality of the model fit, remaining within ± 2% across the full frequency range.

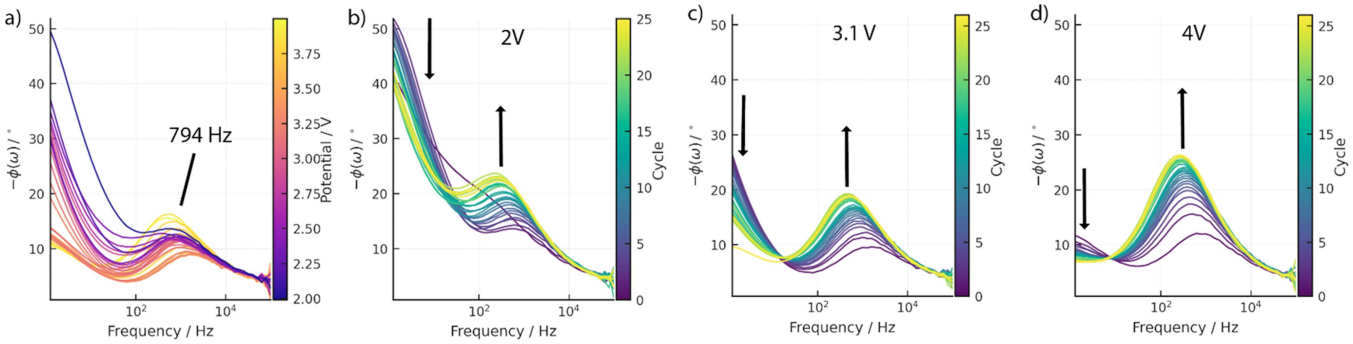

FIGURE 4 | Evolution of Bode-phase response with potential and cycle. (a) Phase-angle spectra across the full voltage window with a distinct feature near ~794 Hz. (b–d) Phase-angle spectra at fixed potentials (2, 3.1, 4 V) colored by cycle index; mid-frequency peaks grow and shift to lower frequency with aging (up-arrows), while low-frequency phase decreases (down-arrows), consistent with interfacial resistance growth and anode-side contact loss.

aggregated across the full voltage window (Figure 4a), the distinct feature emerges near 794 Hz, again consistent with an interfacial relaxation.

The shift of the mid-frequency peak toward lower frequencies reflects an increase in the characteristic relaxation time of the associated interfacial process. Physically, this behavior arises from the growth of interfacial resistance during cycling, which increases the RC time constant and slows the electrochemical response. As degradation progresses, processes that initially occur at higher frequencies therefore shift systematically to lower frequencies, providing a direct spectral signature of interfacial evolution.

In contrast, the low-frequency region exhibits a more complex and non-monotonic evolution. This region reflects a superposition of multiple slow processes, including interfacial capacitance, ion transport limitations, and electrode contact effects. While some contributions—such as increasing interfacial resistance—tend to increase impedance, others—such as redistribution of current pathways or changes in effective capacitance—can reduce the apparent impedance. As a result, the net low-frequency response does not follow a simple monotonic trend with cycling and cannot be uniquely attributed to a single physical process.

This interpretation is supported by the evolution of the R_3 parameter (Figure 5), associated with the anode–electrolyte interface. R_3 increases with cycling and at lower potentials, indicating progressive interfacial degradation. However, the absence of a direct one-to-one correspondence between R_3 and the low-frequency spectral response highlights a key limitation of equivalent-circuit analysis: a single circuit element cannot

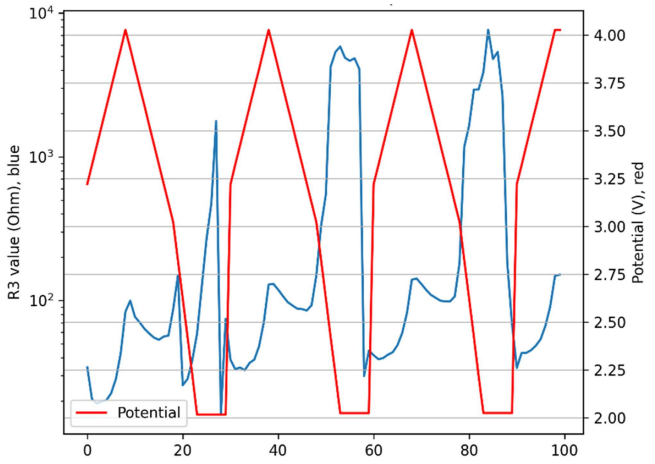

FIGURE 5 | Evolution of the R_3 interfacial resistance parameter as a function of potential over the first four cycles. R_3 (blue) is shown together with the measured potential profile (red). Lower potential corresponds to higher interfacial resistance, and a progressive increase in R_3 is observed with cycling.

fully capture the coupled and evolving processes that dominate this frequency range.

Figure 5 further illustrates these trends by showing the evolution of R_3 as a function of potential over the first four cycles, based on 100 individual EIS spectra. A clear correlation is observed between lower potentials and increased interfacial resistance, together with a progressive rise in R_3 with continued cycling. This confirms that interfacial degradation is strongly potential-dependent and accumulates over repeated cycling.

Importantly, the present analysis focuses on early-cycle evolution, where impedance changes are most pronounced and reproducible, and where equivalent-circuit parameters remain physically interpretable. Extending this analysis to long-term cycling becomes increasingly challenging due to the computational cost of fitting large numbers of spectra and the growing non-uniqueness of equivalent-circuit representations as processes overlap and evolve. In this context, the observed spectral trends—particularly the systematic evolution of peak position and magnitude—provide a more robust and direct descriptor of interfacial dynamics.

Together, these results demonstrate that the geometry of the impedance response itself encodes the relevant electrochemical information, without requiring strict assignment to individual circuit elements. This principle underpins the NEVORA framework, which leverages feature-based representations of the full spectrum to track interfacial evolution in a consistent and model-independent manner.

1.6 | Distribution of Relaxation Times (DRT), ECM, and Feature-Based Impedance Analysis

To further assess model-based impedance analysis under operando conditions, we performed DRT analysis across the full voltage window during the first cycle (Figure 6).

The normalized DRT heat maps (Figure 6a,c) reveal that the impedance response evolves continuously with state of charge, with both the number and position of relaxation processes changing throughout cycling. During each half-cycle (2.0–4.0 V, Figure 6a), up to five distinguishable processes are observed when the SoC is above 3.0 V, whereas when the SoC is below 3.0 V, the response simplifies to approximately three dominant contributions. This evolution indicates that the electrochemical system does not operate as a fixed set of discrete processes, but rather as a dynamically evolving distribution of relaxation times.

This behavior is further reflected in the equivalent-circuit models derived from the DRT analysis (Figure 6b,d). At high state of charge (> 3.0 V, Figure 6b), a circuit comprising five resistive elements is required to capture the observed features, whereas at lower potentials (< 3.0 V, Figure 6d), a reduced three-process model is sufficient. The need to modify circuit topology as a function of electrochemical state highlights a fundamental limitation of equivalent-circuit modeling: the assumption of a fixed number of independent processes is not strictly valid under operando conditions. As processes emerge, merge, or shift in characteristic timescale, parameter assignment becomes ambiguous and model selection inherently non-unique.

DRT analysis alleviates the need to predefine circuit topology by representing the impedance as a continuous distribution over relaxation times. However, as shown in Figure 6e–g, the interpretability of this distribution is itself state-dependent. Bayesian DRT analysis reveals that confidence intervals associated with the relaxation peaks vary significantly with potential. At low potential (2.0 V, Figure 6e), peaks are well-defined with narrow confidence intervals, indicating robust separation of processes. At intermediate potential (3.1 V, Figure 6f), partial overlap emerges, and uncertainty increases. At high potential (4.0 V, Figure 6g), broad confidence intervals indicate substantial ambiguity, reflecting overlapping or poorly resolved processes. These results demonstrate that while DRT provides a more flexible representation than ECM, the identification and interpretation of individual processes are not uniformly reliable across operating conditions.

In contrast, the NEVORA framework does not attempt to decompose the impedance spectrum into discrete circuit elements or relaxation distributions. Instead, it treats the spectrum as a high-dimensional object and extracts physically meaningful descriptors that capture its global geometry. This approach avoids assumptions regarding process count, separability, or stability, enabling a consistent representation of the electrochemical state across all potentials and cycling conditions. By learning direct mappings between spectral features and electrochemical state, the model retains sensitivity to interfacial evolution while remaining robust to the non-uniqueness inherent in ECM and DRT representations.

Together, these results highlight a fundamental distinction in impedance analysis approaches: ECM provides discrete but topology-dependent representations; DRT provides continuous but state-dependent and uncertainty-limited representations; and feature-based methods such as NEVORA provide geometry-based representations that remain consistent under operando conditions.

1.7 | Design Choices That Promote Robustness

Three aspects of the workflow are worth emphasizing:

1. *Feature construction balances physics and pragmatism.* NEVORA includes simple counts (e.g., $N_{|Z|>100\,\Omega}$)

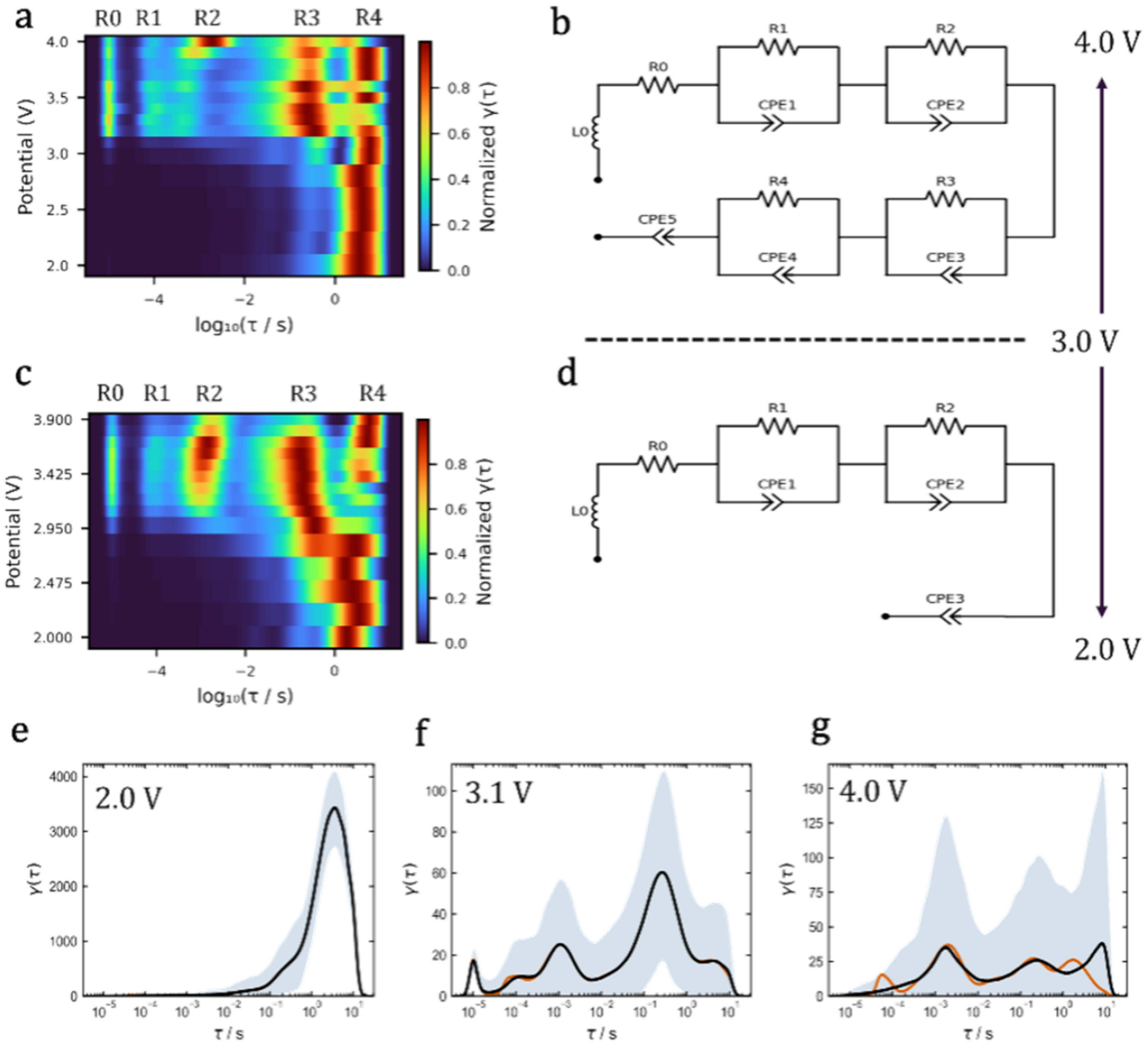

FIGURE 6 | In situ EIS analysis of a sulfide solid-state battery over the 2.0–4.0 V window. (a) Normalized DRT heat map during the first charge half-cycle (2.0–4.0 V). (b) Equivalent circuit model derived from DRT analysis at high state of charge (> 3.0 V), comprising five resistive processes. (c) Normalized DRT heat map during the first discharge half-cycle (4.0–2.0 V). (d) Equivalent circuit model derived from DRT analysis at low state of charge (< 3.0 V), reduced to three resistive processes. (e–g) Bayesian-DRT analysis at selected potentials: (e) 2.0 V, (f) 3.1 V, and (g) 4.0 V, showing the evolution of confidence intervals associated with the DRT distribution. DRT, distribution of relaxation times; EIS, electrochemical impedance spectroscopy.

alongside more refined integrals and extrema. The former are surprisingly powerful for early fault detection and require almost no computation; the latter support precise SoC regression. This mix prevents over-reliance on any single delicate quantity.

2. *Context matters*. Attaching the instantaneous voltage, SoC/Cycle estimates from the galvanostatic record, and the carried-in relative charge/discharge time to each EIS block gives the model a time-aware prior.

3. *Multi-output learning captures co-structure*. Training SoC and cycle number together encourages the model to exploit shared dependencies in the features.

1.8 | From Laboratory Demonstration to Embedded SSBMS

The immediate implication would be a path to on-board diagnostics that can run on microcontrollers or edge devices. The computational budget is lightweight: feature extraction is a handful of arithmetic operations; inference with an RF or GB model requires only tree traversals. However, the question remained about how lightweight the measurement budget could be and still produce exceptional results. Therefore, the models were retrained with only the five top features determined from the Random Forest regressor (Potential, Phase_21, Phase_13, Zmag_1, and Phase_44). Subsequently, the tested

TABLE 2 | Performance of machine-learning models trained using a reduced feature set comprising only the potential, Phase_21, Phase_13, Zmag_1, and Phase_44 parameters. Both Random Forest and gradient boosting regressors maintain excellent predictive accuracy for state of charge (SoC) and cycle number, achieving $R^2 > 0.98$ and mean absolute errors (MAE) below 1%, demonstrating that a minimal subset of electrochemical impedance spectroscopy (EIS)-derived features can effectively capture the electrochemical state evolution.

Model	Target	R^2	MAE
Random Forest	SoC (%)	0.993	0.886
Random Forest	Cycle	0.987	0.990
Gradient boosting	SoC (%)	0.994	0.987
Gradient boosting	Cycle	0.992	0.989

data set produced $R^2 > 0.98$ with MAE below 1% and exhibited in Table 2, thus demonstrating that even only five data points are sufficient for highly accurate predictors applied to solid-state batteries.

By limiting the measurement budget to only a few primary data points in mid-frequency ranges, diagnostic measurements can be limited to milliseconds. While full-spectrum EIS acquisition remains inherently time-limited, this result demonstrates that once sparse-frequency measurements are available, inference can be performed at millisecond timescales, highlighting a pathway toward fast impedance-based diagnostics. Altogether, this makes a compelling case for integrating EIS-based diagnostics into early SSB prototypes and pilot lines.

1.9 | Limitations and Opportunities

As with any data-driven method, generalization beyond the trained distribution must be verified. Three axes matter most: chemistry, temperature, and mechanical boundary conditions (pressure, stack design). The features we use are intentionally generic, and the physical picture (interfacial arcs dominate) is broadly valid across sulfides, oxides and halides but transfer across chemistries should be validated experimentally. Temperature shifts characteristic frequencies; modest domain adaptation or temperature as an explicit model input should mitigate this. Mechanical pressure affects contact and therefore R_2 and R_3; including pressure readouts or features derived from high-frequency inductive response would improve robustness. Feature distributions and model predictions are expected to shift with operating conditions such as temperature, pressure, and electrode architecture. Temperature primarily affects relaxation times (frequency scaling), while pressure influences interfacial contact and resistance evolution. Electrode design alters transport pathways within composite structures. To address this, the framework can incorporate these variables as additional inputs or apply domain adaptation techniques.

Finally, while RF/GB models already meet accuracy targets, probabilistic or conformal variants could deliver calibrated uncertainty [9]—useful for SSBMS decisions that blend model outputs with safety margins. Future work could benefit from sequential modeling approaches, including recurrent neural networks and transformer-based architectures, to explicitly incorporate temporal dependencies between successive impedance measurements.

1.10 | Reproducibility and Data Pathway

The entire analysis pipeline—from classification of galvanostatic versus EIS rows, to cycle indexing by current-sign transitions, to feature construction and multi-output regression—was implemented in Python with standard libraries. Feature vectors and trained models are serialized for reuse; diagnostic plots (e.g., predicted vs true, feature importance) are generated automatically for quality control. Because the method used by NEVORA consumes only derived features, it is compatible with privacy-preserving or bandwidth-limited deployments: raw spectra need not leave the device.

1.11 | Broader Relevance

Although demonstrated here on a sulfide/NMC solid-state battery, the impedance-based modeling framework is broadly transferable to any electrochemical or physicochemical system measurable by EIS. The same principles can be applied to halide and oxide solid electrolytes, silicon or lithium-metal composite electrodes, and sodium- or magnesium-based cells. Beyond batteries, this approach can extend to fuel cells, supercapacitors, solid oxide electrolyzers, corrosion and coating diagnostics, and even bioelectrochemical systems where impedance spectra encode interfacial or transport phenomena. In manufacturing, brief impedance snapshots during stack assembly or formation could serve as rapid quality control metrics to identify poor contact, contamination, or nonuniform interfaces before costly cycling or device integration.

2 | Conclusions

We demonstrate that coupling in situ EIS with machine learning provides a practical and interpretable diagnostic framework for solid-state batteries. By encoding spectra into mathematical feature vectors and training lightweight multi-output models, we achieve accurate, real-time predictions of SoC and cycle index without relying on fragile equivalent-circuit fits. Feature-importance analysis and voltage-dependent trends (Figures 1–4) reveal that the models focus on the spectral regions most sensitive to interfacial health—particularly the growth and shift of a mid-frequency phase peak linked to the cathode composite–electrolyte interface, and low-frequency changes indicative of anode contact loss. Moreover, we show that these compact yet robust models retain high predictive accuracy even when trained on a minimal subset of features corresponding to interfacial processes. Together, these results chart a clear path toward impedance-informed battery management systems, where brief EIS blocks acquired opportunistically during operation enable adaptive control strategies that extend lifetime and enhance safety.

Acknowledgments

This research work is part of PIE project "Innovative and Designed (Electro)-Chemistry, All-in-One for Lithium Sulfide Solid Electrolytes"

(IDEAL-Li), reference 20226AT009 supported by The Spanish National Research Council (CSIC). This work was supported by the ELISA project (ref. CNS2023-145494), funded by MCIN/AEI/10.13039/501100011033 and by the European Union «NextGenerationEU»/PRTR.

Disclosure

NEVORA is a proprietary software developed by the Consejo Superior de Investigaciones Científicas (CSIC). Access to third parties will be granted under fair and reasonable conditions taking into account the specific circumstances of the request for access.

Conflicts of Interest

The authors declare no conflicts of interest.

Data Availability Statement

The data that support the findings of this study are available from the corresponding author upon reasonable request.

References

1. Y. Zheng, Y. Shen, J. Guo, et al., "Recent Advances in Solid-State Lithium Batteries Based on Anode Engineering," *Nano Research Energy* 3, no. 3 (2024): e9120118, https://doi.org/10.26599/nre.2024.9120118.

2. X. Yao, D. Liu, C. Wang, et al., "High-Energy All-Solid-State Lithium Batteries With Ultralong Cycle Life," *Nano Letters* 16, no. 11 (2016): 7148–7154, https://doi.org/10.1021/acs.nanolett.6b03448.

3. H. Song, K. Münch, X. Liu, et al., "All-Solid-State Li-S Batteries With Fast Solid-Solid Sulfur Reaction," *Nature* 637, no. 8047 (2025): 846–853, https://doi.org/10.1038/s41586-024-08298-9.

4. Y.-Y. Sun, F. Li, and P.-Y. Hou, "Research Progress on the Interfaces of Solid-State Lithium Metal Batteries," *Journal of Materials Chemistry A* 9, no. 15 (2021): 9481–9505, https://doi.org/10.1039/d1ta00467k.

5. P. Vadhva, J. Hu, M. J. Johnson, et al., "Electrochemical Impedance Spectroscopy for All-Solid-State Batteries: Theory, Methods and Future Outlook," *ChemElectroChem* 8, no. 11 (2021): 1930–1947, https://doi.org/10.1002/celc.202100108.

6. L. Zhang, Y. Dai, C. Li, et al., "Recent Advances in Electrochemical Impedance Spectroscopy for Solid-State Batteries," *Energy Storage Materials* 69 (2024): 103378, https://doi.org/10.1016/j.ensm.2024.103378.

7. C.-Y. Yu, J. Choi, J. Dunham, et al., "Time-Resolved Impedance Spectroscopy Analysis of Aging in Sulfide-Based All-Solid-State Battery Full-Cells Using Distribution of Relaxation Times Technique," *Journal of Power Sources* 597 (2024): 234116, https://doi.org/10.1016/j.jpowsour.2024.234116.

8. Y. J. Kim, H. Jeong, S. Nam, D. Shin, J.-H. Lee, and H. Kim, "Degradation Analysis During Fast Lifetime Cycling of Sulfide-Based All-Solid-State Li-Metal Batteries Using in Situ Electrochemical Impedance Spectroscopy," *Journal of Materials Chemistry A* 13, no. 29 (2025): 23946–23956, https://doi.org/10.1039/d5ta02065d.

9. Y. Xu, A. Liaw, R. P. Sheridan, and V. Svetnik, "Development and Evaluation of Conformal Prediction Methods for Quantitative Structure-Activity Relationship," *ACS Omega* 9, no. 27 (2024): 29478–29490, https://doi.org/10.1021/acsomega.4c02017.

10. Y. Qi, M. W. Swift, E. J. Fuller, and A. A. Talin, "Interface Potentials Inside Solid-State Batteries: Origins and Implications," *MRS Bulletin* 48, no. 12 (2023): 1239–1246, https://doi.org/10.1557/s43577-023-00625-1.

Supporting Information

Additional supporting information can be found online in the Supporting Information section.

Supporting file: bte270122-sup-0001-Supporting_Information_Revised.docx.